Sacrificial-agent-free artificial photosynthesis of hydrogen peroxide over step-scheme WO₃/NiS hybrid nanofibers

Kai Wang [a,c,*], Jingping Li [a], Xiufan Liu [a], Qiang Cheng [a], Yue Du [a], Dian Li [a], Guohong Wang [a], Bin Liu [b,**]

[a] *College of Urban and Environmental Sciences, Hubei Key Laboratory of Pollutant Analysis and Reuse Technology, Huangshi Key Laboratory of Soil Pollution Control, Hubei Normal University, Huangshi 435002, PR China*
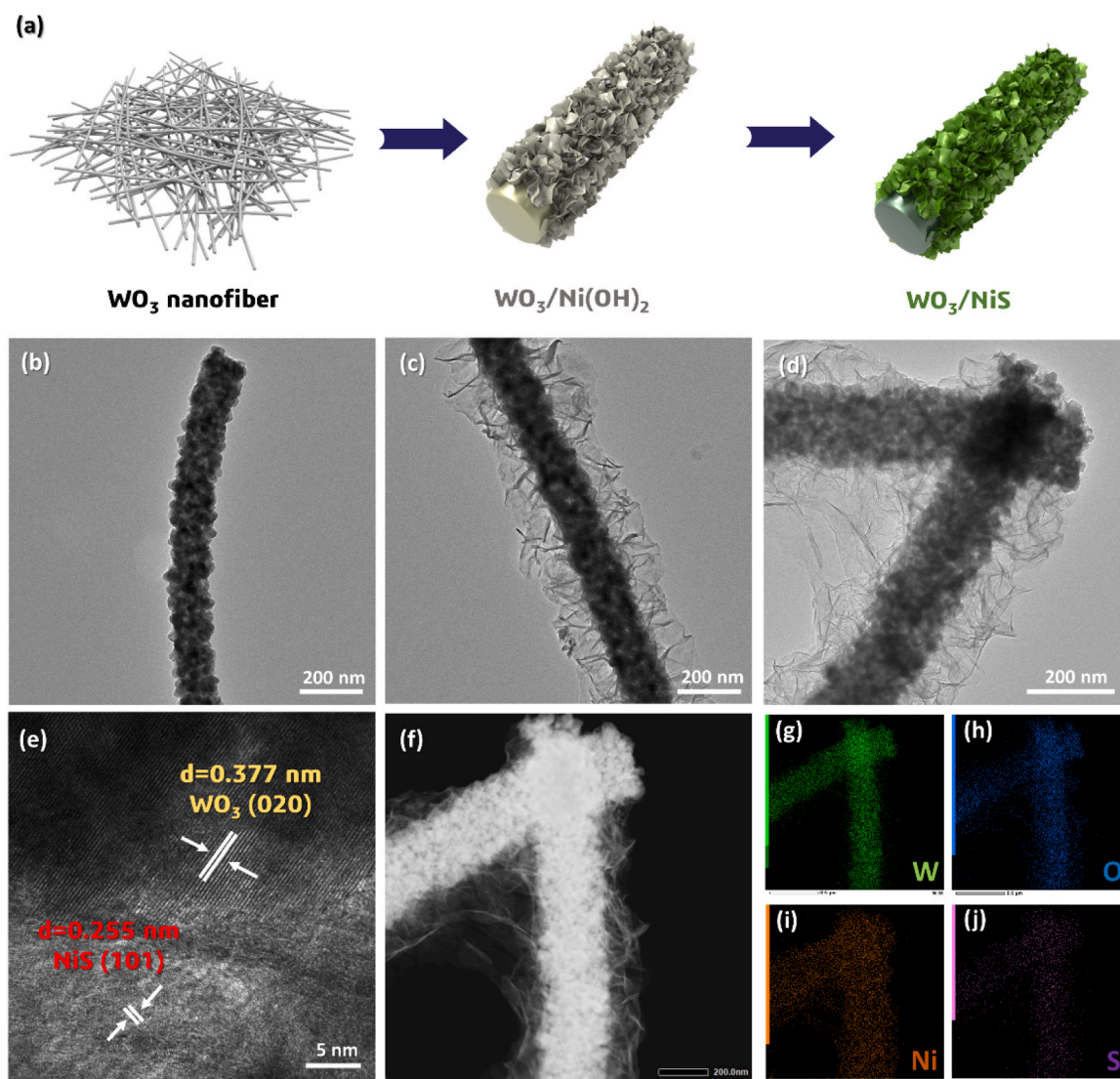[b] *Department of Materials Science and Engineering, City University of Hong Kong, 999077, Hong Kong, China*
[c] *School of Chemistry, Chemical Engineering and Biotechnology, Nanyang Technological University, 62 Nanyang Drive, Singapore 637459, Singapore*

ARTICLE INFO

Keywords:
Hydrogen peroxide
Artificial photosynthesis
Nanofibers
Step-scheme
Sacrificial-agent-free

ABSTRACT

Developing low-cost and durable photocatalysts for sacrificial-agent-free artificial photosynthesis of hydrogen peroxide is challenging. In this work, an all-inorganic hybrid nanofiber step-scheme photocatalyst, WO₃/NiS (WONS), was constructed for efficient generation of hydrogen peroxide in pure water at ambient condition. The optimal photocatalyst, WONS35 % (with 35 wt% of NiS), exhibits remarkable efficiency in producing H₂O₂ at a rate of 2.59 mmol $g_{catalyst}^{-1}$ h^{-1} under visible light illumination, surpassing the H₂O₂ production rate of pristine WO₃ and NiS by 11.3 and 16.7 times, respectively. WONS35 % demonstrates an apparent quantum yield of 4.97 % at a wavelength of 420 nm. The significantly enhanced photocatalytic performance can be ascribed to the synergistic effect of the improved charge separation and transfer induced by the step-scheme pathway and the highly selective two-electron oxygen reduction reaction (ORR) over the hybrid nanofiber photocatalyst.

1. Introduction

Hydrogen peroxide (H₂O₂) is an important green oxidant, which has been extensively used in chemical manufacturing, electronics, organic synthesis, wastewater treatment, etc. [1–8]. In China, the total annual production of H₂O₂ in 2021 was 12.39 million tons, primarily based on energy-intensive, pollutive, and expensive anthraquinone process [9–15]. It is therefore highly imperative to develop a cost-effective and environmentally friendly method for making H₂O₂. Artificial photosynthesis of H₂O₂ has attracted increasing attention over the past few years, as it only requires water, air, sunlight and a suitable photocatalyst [16–24]. However, the low efficiency of charge separation/transfer in the photocatalyst and the poor H₂O₂ selectivity still greatly limit the productivity of H₂O₂ in the photocatalytic reaction [25–31].

To tackle the aforementioned challenge, considerable endeavors have been focused on the advancement of semiconductor heterostructures with the aim of augmenting charge separation and transfer. This is substantiated by the observed enhancement in photocatalytic

activity through experimental means. Despite the apparent excellence of type-II charge transfer in achieving efficient charge separation, a closer examination reveals certain deficiencies from both thermodynamic and dynamic perspectives. Since 2001, researchers have been gradually developing a direct Z-scheme photocatalyst without the need for a solid electronic conductor or redox ion couple. To overcome the challenges and errors associated with charge transfer in type-II heterojunctions, traditional Z-scheme systems, and all-solid-state Z-scheme systems, a new concept known as the step-scheme (S-scheme) heterojunction photocatalysts has emerged. This concept builds upon the advantages of the direct Z-scheme heterojunction and offers several benefits. [31–33]. The interfacial internal electric field (IEF) generated in the S-scheme photocatalyst can ensure efficient separation of photogenerated charge carriers, while retaining their high redox power. This is beneficial for achieving optimal photocatalytic reactivity [33–45]. On the other hand, the poor H₂O₂ selectivity in artificial photosynthesis can be improved by regulating the oxygen reduction reaction (ORR) kinetics [46–48].

In this work, step-scheme WO₃/NiS hybrid nanofiber photocatalysts

---

Fig. 1. (a) Schematic diagram showing the preparation steps of WO$_3$/NiS hybrid nanofibers. TEM image of (b) WO$_3$ nanofibers, (c) WO$_3$/Ni(OH)$_2$ and (d) WO$_3$/NiS hybrid nanofibers. (e) HRTEM image of WO$_3$/NiS hybrid nanofibers. (f) HAADF-STEM image of WO$_3$/NiS hybrid nanofibers, and the corresponding EDX mapping images of (g) W, (h) O, (i) Ni, and (j) S.

were successfully designed and synthesized based on an electrospinning plus hydrothermal method. Thanks to the one-dimensional (1D) nano-structure and step-scheme charge transfer pathway studied by density functional theory (DFT) and in-situ diffusion reflectance infrared Fourier transform spectroscopy (DRIFTS), the optimal WONS35 % photocatalyst exhibited a stable H$_2$O$_2$ production rate as high as 0.619 mmol $g_{catalyst}^{-1}$ h^{-1} under visible light illumination in pure water at ambient condition. This work provides a feasible strategy to design noble-metal-free het-erostructures for artificial photosynthesis of H$_2$O$_2$.

2. Experimental

2.1. Synthesis of photocatalysts

The details of synthesis are shown in Text S1 of the Supplementary Materials.

2.2. Characterization

The physical and chemical properties of the as-prepared photo-catalysts were characterized by XRD, SEM, TEM, Raman spectroscopy,

FT-IR, ESR, BET, UV–vis DRS, SPV, and in-situ DRIFTS. The contents of characterization are described in Text S2 of the Supplementary Materials.

2.3. DFT calculation

DFT calculations were performed in the Vienna ab initio simulation package (VASP). The details of calculation methodology are shown in Text S3 of the Supplementary Materials.

2.4. Photocatalytic H$_2$O$_2$ production

In a typical reaction, 20 mg of photocatalyst and 60 mL of ultra-pure water were added into a 100 mL three-neck flask reactor. The bottle was kept in a temperature-controlled air bath at 25 ± 0.5 °C with wind flow and was irradiated using a 300 W Xenon lamp (PLS-SXE300D, Beijing Perfectlight) equipped with a UV cutoff filter (420–780 nm). During photoreaction, 2 mL of solution was sampled every 30 min and filtered by a 0.17 μm microporous filter to remove the photocatalyst. The con-centration of H$_2$O$_2$ was determined by iodimetry [49]. The apparent quantum yield (AQY) for H$_2$O$_2$ production was measured using
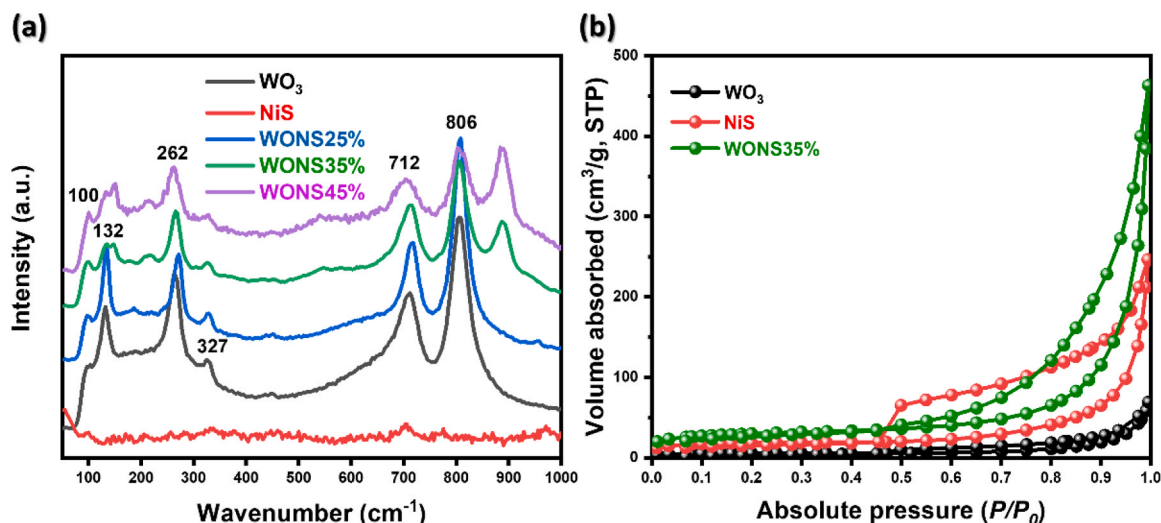
Fig. 2. (a) Raman spectra of WO$_3$, NiS, WONS25 %, WONS35 %, and WONS45 %. (b) Nitrogen adsorption-desorption isotherms of WO$_3$, NiS and WONS35 %.

monochromatic light (LED, 420 nm) and calculated using the following formula [Eq. (1)]:

$$AQY(\%) = \frac{2 \times M \times h \times c \times N_A}{S \times P \times t \times \lambda} \times 100\%$$ (1)

Where, M represents the amount of produced H$_2$O$_2$ molecules, N$_A$ is the Avogadro constant, h represents the Planck constant, c is the speed of

light, S is the irradiation area, P is the intensity of irradiation light, t is the photoreaction time, λ is the wavelength of the incident monochromatic light.

2.5. Photoelectrochemical tests

Electrochemical measurements were measured on an

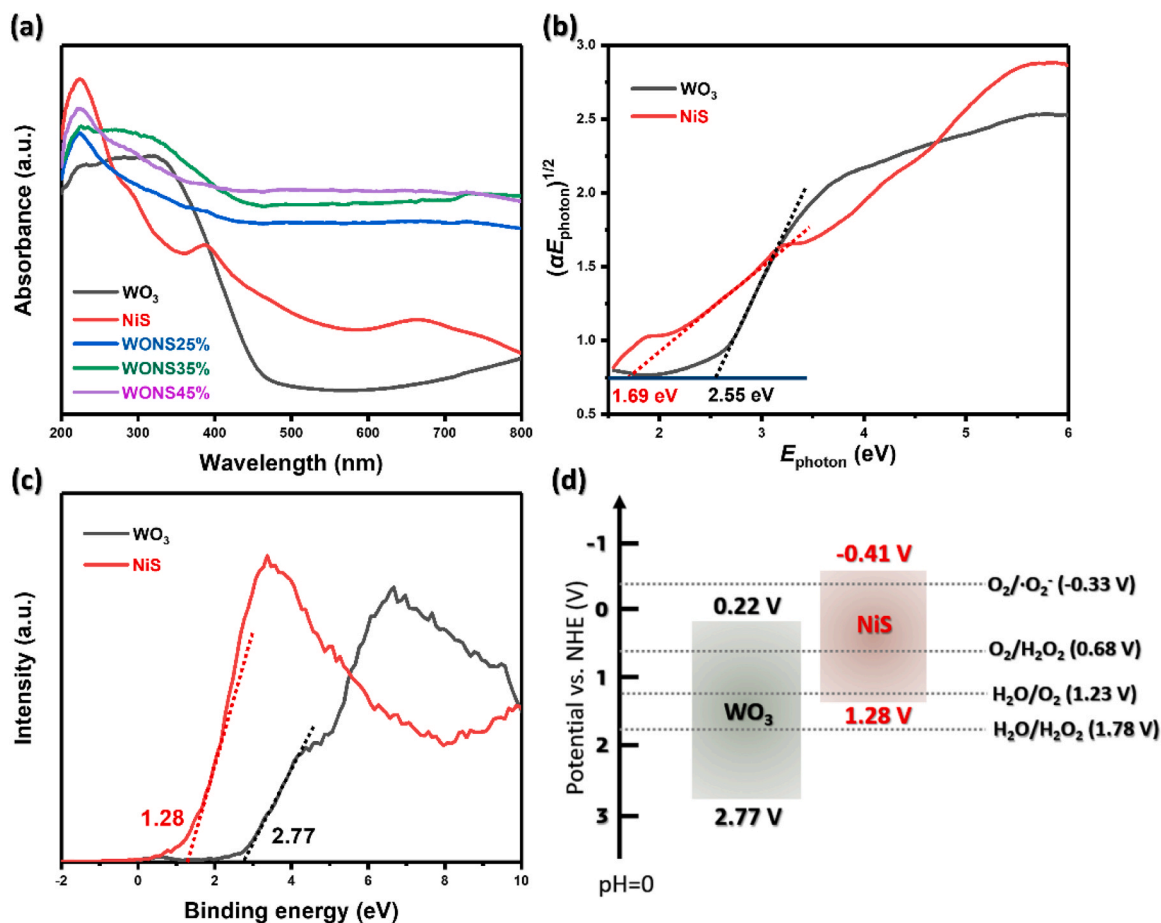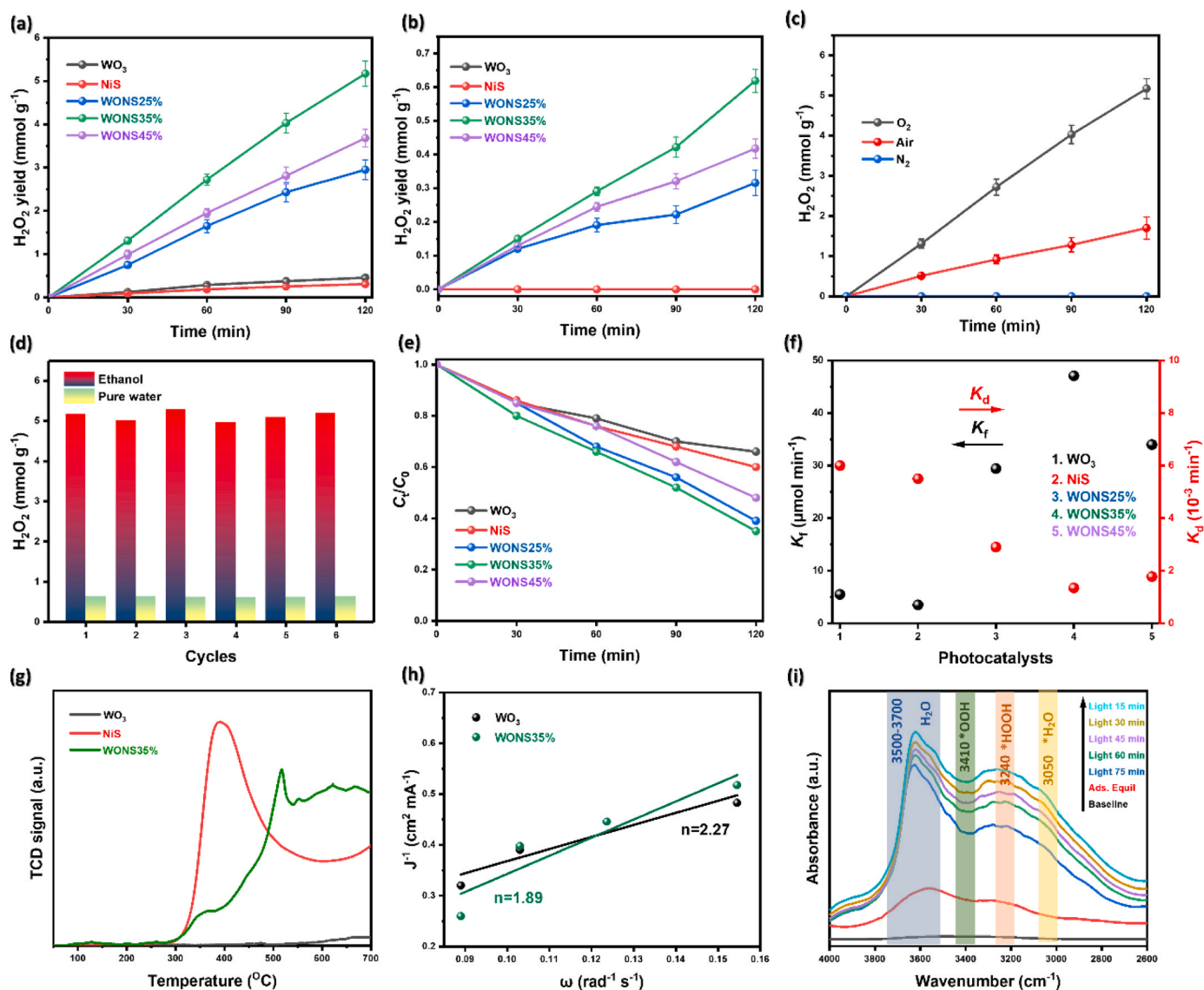Fig. 3. (a) UV–vis diffuse reflectance spectra of WO$_3$, NiS, WONS25 %, WONS35 %, and WONS45 %. (b) Tauc plots. (c) VB-XPS spectra and (d) band structure of WO$_3$ nanofibers and NiS nanosheets.

Fig. 4. Photocatalytic H_2O_2 production over the as-prepared photocatalysts in the presence of (a) ethanol as a sacrificial reagent and (b) in pure water. (c) Photocatalytic H_2O_2 production over WONS35 % in different atmospheres. (d) Cyclic photocatalytic H_2O_2 production over WONS35 %. (e) Decomposition of H_2O_2 (1 mM) under light illumination over different as-prepared photocatalysts. (f) The calculated formation rate constant (K_f) and decomposition rate constant (K_d) of H_2O_2. (g) O_2-TPD signals of WO_3, NiS, and WONS35 %. (h) Koutecky-Levich plots for WO_3 and WONS35 %. (i) *In-situ* DRIFTS spectra recorded over WONS35 % under visible light irradiation.

electrochemical workstation (CHI660E, China). The details of photo-electrochemical tests are shown in Text S4 of the Supplementary Materials.

3. Results and discussion

3.1. Morphological and structural characterizations

Fig. 1a shows the synthesis steps to prepare WO_3/NiS hybrid nanofibers. In the first step, electrospun WO_3 precursors were calcined to obtain WO_3 nanofibers. Subsequently, $Ni(OH)_2$ nanosheets were grown on the surface of WO_3 nanofibers by a hydrothermal method, yielding WO_3/$Ni(OH)_2$ hybrid nanofibers, which were then transformed into WO_3/NiS hybrid nanofibers via an ion-exchange process [50–53]. The morphological information of the as-prepared samples was examined by TEM and HRTEM. Fig. 1b shows that pristine WO_3 nanofibers are made of interconnected nanoparticles, with an average length and diameter of several micrometers and 150 nm, respectively. Following hydrothermal

reaction, numerous $Ni(OH)_2$ nanoflakes were found uniformly grown on the surface of WO_3 nanofibers (Fig. 1c). The subsequent ion-exchange process did not change the sample morphology (Fig. 1d). As displayed in Fig. 1e, the HRTEM image of WO_3/NiS hybrid nanofibers with 35 wt % NiS (WONS35 %) shows clear lattice fringes with d spacings of 0.377 nm and 0.255 nm, representing the WO_3 (020) facets and rutile NiS (101) facets, respectively, indicating the presence of both WO_3 and NiS phases. Moreover, the EDX mapping images of WONS35 % (Fig. 1f–j) show coexistence of W, O, Ni, and S elements, which are uniformed distributed, forming a one-dimensional core-shell nanostructure.

X-ray diffraction (XRD) was performed to examine the crystal structure of the as-prepared catalysts. The main peaks of WO_3 (JCPDS No. 20-1324) were identified at 23.1°, 23.7°, 24.1°, 26.0°, 26.6°, 28.8°, and 33.3°, which correspond to the (001), (020), (200), (011), (120), (111), and (021) planes of monoclinic WO_3 (refer to Fig. S1). Due to the low content of NiS, no clear diffraction peaks of NiS could be observed in WONS samples. The predominant vibrational modes of WO_3
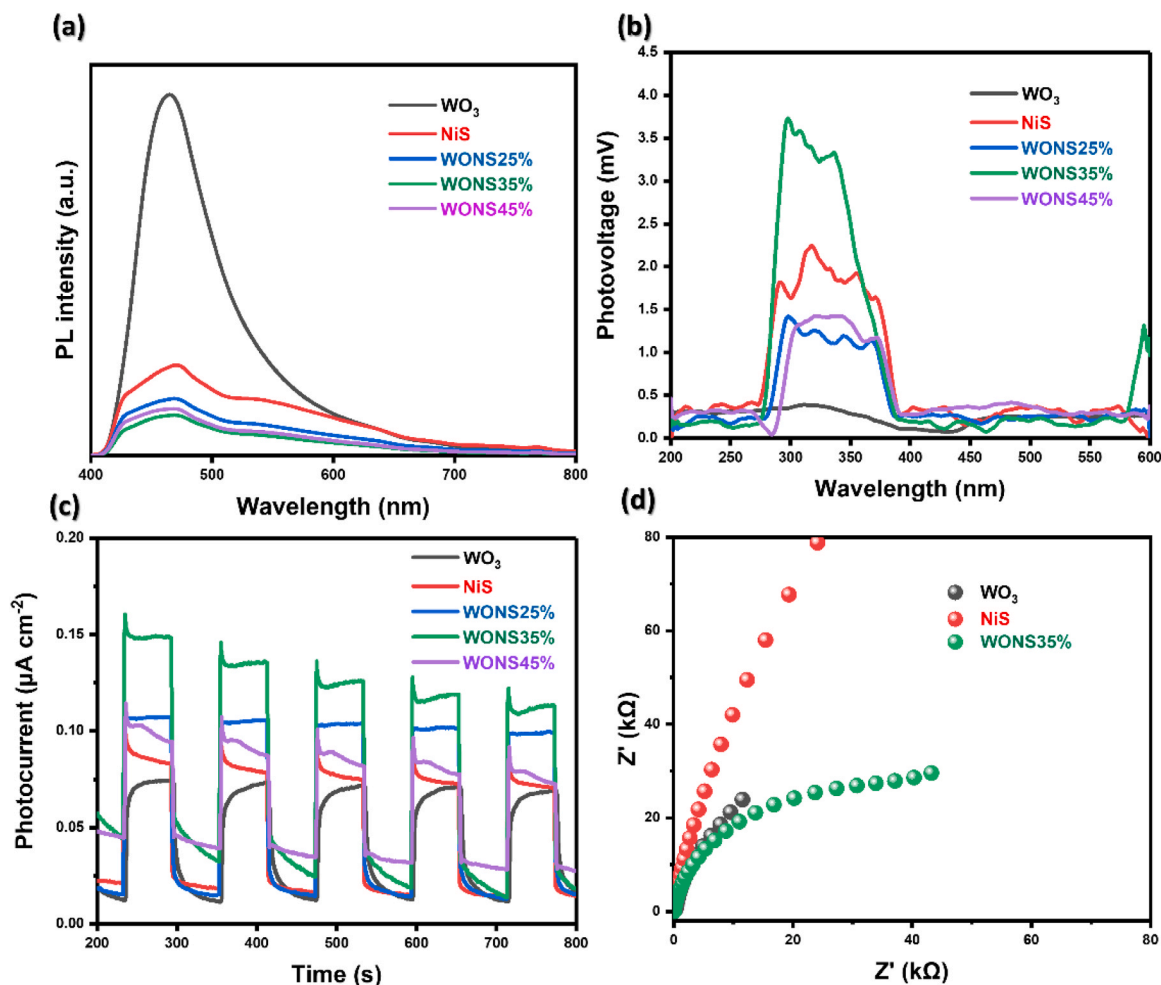
Fig. 5. (a) PL spectra. (b) TRPL spectra. (c) Transient photocurrent response. (d) EIS spectra of WO$_3$, NiS, and WONS35 %.

and WONS samples (refer to Fig. 2a) were identified by Raman spectroscopy at 806, 712, and 262 cm^{-1}, which can be attributed to stretching of O−W−O, stretching of W−O, and bending of O−W−O, respectively. Moreover, Raman bands were observed below 200 cm^{-1} (such as at 100 and 132 cm^{-1}) in all samples, indicative of low-frequency phonon mode markers linked to temperature variations. WO$_3$ nanofibers, NiS nanosheets, and WONS35 % all exhibit type-IV isotherms with a type-H3 hysteresis loop, indicating presence of slit-shaped macropores. Notably, the specific surface area (S$_{BET}$) of WONS35 % (97.23 m^2 g^{-1}) is about 5.7 and 1.7 times that of pristine WO$_3$ nanofibers (16.86 m^2 g^{-1}) and NiS nanosheets (56.98 m^2 g^{-1}).

The optical properties and band structure information of the as-prepared samples were studied by UV–vis absorption spectroscopy and X-ray photoelectron spectroscopy (XPS) (Fig. 3). The UV–vis spectrum in Fig. 3a reveals that pristine WO$_3$ nanofibers can absorb both ultraviolet and visible light with wavelengths up to 500 nm, whereas NiS displays strong absorption of visible light owing to its narrow bandgap. With increase in NiS loading on WO$_3$ nanofibers, the WO$_3$/NiS hybrid nanofibers exhibited a slight improvement in light harvesting within the visible light range. The band structure was determined by Tauc plot and valence band X-ray photoelectron spectroscopy (VB-XPS), and the bandgap and VB position of WO$_3$ and NiS were estimated to be 2.55 and 1.69 eV and 2.77 and 1.28 V vs. NHE, respectively (Fig. 3b), based on which, the conduction band potential (E$_{CB}$) of WO$_3$ nanofibers and NiS nanosheets were determined to be 0.22 and − 0.41 V vs. NHE (Fig. 3c). The band structures of WO$_3$ and NiS are illustrated in Fig. 3d. Despite having a narrower bandgap that is beneficial for light absorption, NiS displays a weaker oxidation potential of photogenerated holes. By

combining WO$_3$ nanofibers with NiS nanosheets via a seamless contact heterojunction, this can greatly enhance the redox ability of the photogenerated charge carriers.

3.2. Photocatalytic H$_2$O$_2$ evolution

The photocatalytic oxygen reduction reaction (ORR) to produce H$_2$O$_2$ over the as-prepared samples was assessed in the presence of ethanol as a hole scavenger. Under Xenon lamp illumination, the WO$_3$ nanofibers showed a very low H$_2$O$_2$ production rate (0.229 mmol g$_{catalyst}^{-1}$ h^{-1}), which might be due to the low conduction band edge of WO$_3$ to reduce O$_2$ to •O$_2^-$. On the other hand, the NiS nanosheets alone also exhibited a low H$_2$O$_2$ production rate (0.155 mmol g$_{catalyst}^{-1}$ h^{-1}) even in the presence of a hole scavenger. In contrast, decorating NiS nanosheets on WO$_3$ nanofibers greatly increased the H$_2$O$_2$ production rate under Xenon lamp illumination (Fig. 4a). In particular, the WONS35 % reached a H$_2$O$_2$ production rate of 2.59 mmol g$_{catalyst}^{-1}$ h^{-1}, which is about 11.3 and 16.7 times higher than that of pristine WO$_3$ and NiS, respectively. It is worth noting that the WONS35 % even could reduce O$_2$ in pure water (Fig. 4b) to produce H$_2$O$_2$ under visible light irradiation with a H$_2$O$_2$ production rate of 0.619 mmol g$_{catalyst}^{-1}$ h^{-1}. The apparent quantum yield (AQY) for H$_2$O$_2$ production over WONS35 % at 420 nm was determined to be 4.98 % and 0.60 % in the presence and absence of ethanol. Additionally, the photocatalytic reaction was performed in different atmospheres (Fig. 4c), and H$_2$O$_2$ could only be produced in O$_2$ atmosphere, indicating the 2e$^-$ ORR pathway towards generating H$_2$O$_2$.

Besides activity, the photocatalytic stability is equally important. In
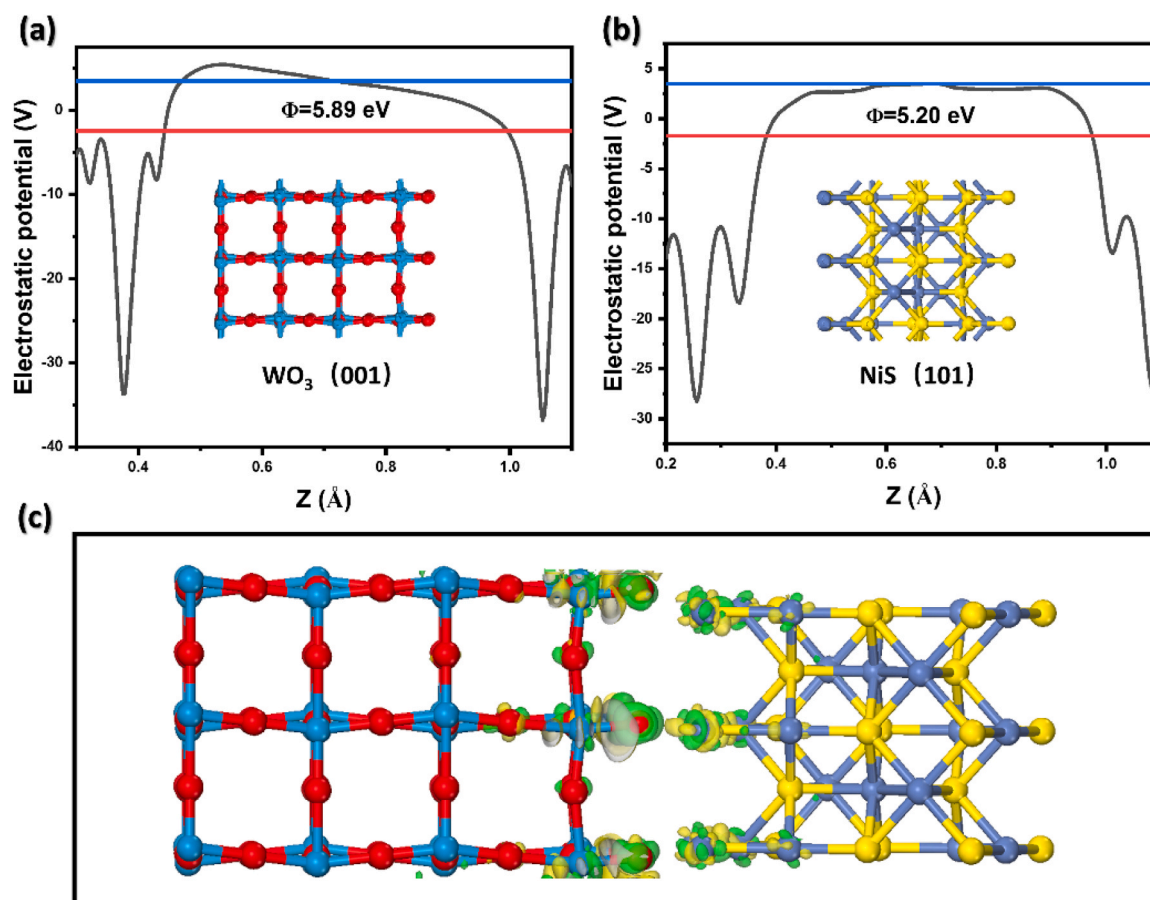
Fig. 6. (a) The calculated electrostatic potential for (a) the (001) facet of WO$_3$ and (b) the (101) facet of NiS. (c) Charge density difference of WO$_3$/NiS heterojunction.

six cycles of photocatalytic reaction, the WONS35 % photocatalyst shows negligible decrease in H$_2$O$_2$ production rate (Fig. 4d). The production of H$_2$O$_2$ in photocatalysis is a dynamic process, during which, H$_2$O$_2$ can be produced and then decomposed due to the reaction between H$_2$O$_2$ and the photogenerated electrons or holes. As shown in Fig. 4e, all of the as-prepared photocatalysts show very low H$_2$O$_2$ decomposition rate under light illumination. The rate constant for H$_2$O$_2$ generation (K$_f$, μM min^{-1}) and decomposition (K$_d$, min^{-1}) were calculated based on zero-order and first-order kinetics, respectively [50,54]. The values of K_f and K_d are estimated by the fitting data in Fig. 4a and [Eq. (2)].

$$[H_2O_2] = K_f/K_d \times \{1 - \exp(-K_d \times t)\} \tag{2}$$

Based on the fitting data as shown in Fig. 4f, the optimal WONS35 % photocatalyst displays a highest K_f value and a moderate K_d value, leading to a significant increase in H$_2$O$_2$ formation and suppression of H$_2$O$_2$ decomposition. Additionally, compared with pure WO$_3$ and NiS, WONS35 % displays higher O$_2$ desorption temperatures (Fig. 4g), revealing stronger O$_2$ adsorption over WONS35 %. To study oxygen reduction catalysis, the oxygen reduction reaction (ORR) linear sweep voltammetry (LSV) curves were recorded as shown in Fig. S3a-b, where current density increases with rotation speed. The current density combines a mixture of diffusion-controlled and reaction-controlled mechanisms. Based on Koutecky-Levich (K-L) fitting (Fig. 4h) [50], the average number of electron transfer (n) for ORR was calculated to be 2.27 and 1.89 over WO$_3$ and WONS35 %, respectively, indicating favorable 2e$^-$ ORR pathway on the as-prepared WONS catalysts. *In-situ* DRIFTS was performed to monitor the real-time formation of H$_2$O$_2$ on WONS35 %. The infrared spectra were recorded under visible light

illumination after reaching adsorption equilibrium, as depicted in Fig. 4i. The peak observed at 3410 cm^{-1} is associated with *OOH vibration, indicating the generation of H$_2$O$_2$ via a two-electron ORR process [50]. Additionally, another emerged peak at 3240 cm^{-1} can be attributed to the O-H stretching in the produced H$_2$O$_2$. These results directly validate the generation of H$_2$O$_2$ over WONS35 % under irradiation.

3.3. Photocatalytic mechanism

To probe the photocatalytic H$_2$O$_2$ production reaction, the separation and transfer efficiency of photogenerated charge carriers were first investigated by photoluminescence (PL) spectroscopy. Fig. 5a shows the PL spectra of WO$_3$, NiS, and WO$_3$/NiS composites with different NiS contents (WONS25 %, WONS35 % and WONS45 %). It can be observed that introduction of NiS over WO$_3$ can effectively reduce the recombination of photogenerated electrons and holes. To further probe charge separation, surface photovoltage (SPV) spectroscopy was performed. As shown in Fig. 5b, a surface photovoltage response in the wavelength range from 300 to 400 nm was observed over the WO$_3$/NiS composite, and WONS35 % displays the highest surface photovoltage intensity, indicating the lowest recombination rate of photogenerated electrons and holes in WONS35 % [55,56]. Fig. 5c compares the photocurrent signal of different samples measured under chopped light illumination. Among all samples, WONS35 % produces the highest photocurrent density, suggesting efficient generation and transfer of photoexcited carriers in WONS35 %. This can be further confirmed by the electrochemical impedance spectroscopy (EIS) measurements as shown in Fig. 5d, where WONS35 % exhibits the smallest semicircle, indicating the most efficient electron transfer.
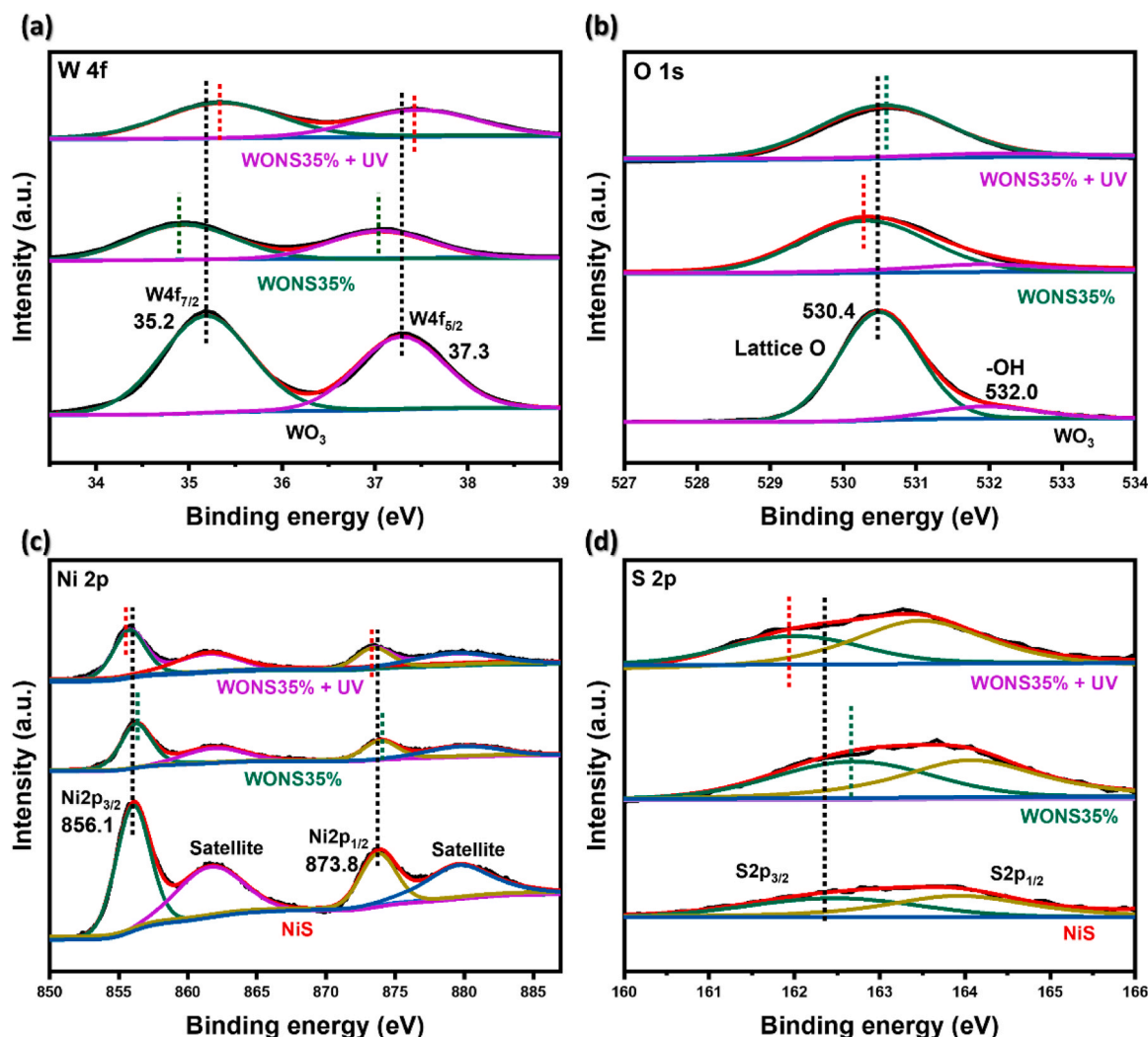
Fig. 7. XPS spectra of (a) W 4f and (b) O 1s of WO_3 and WONS35 %. XPS spectra of (c) Ni 2p and (d) S 2p of NiS and WONS35 %.

The difference in Fermi energy (E_F) between two materials determines the direction of electron migration. At the interface between two semiconductors, electrons tend to move from the semiconductor with a higher E_F to another with a lower E_F. Density functional theory (DFT) was applied to calculate the work functions of WO_3 and NiS, which were found to be 5.89 and 5.20 eV, respectively (as shown in Fig. 6a-b). These values indicate that NiS has a higher Fermi energy level than WO_3. Once a junction is formed between NiS and WO_3, electrons tend to move from NiS to WO_3 that generates an internal electric field at the WO_3/NiS interface, pointing from NiS to WO_3. As depicted in Fig. 6c, the green regions representing charge accumulation are mainly located over WO_3, while the majority of the yellow regions representing charge depletion are observed on NiS [57–59]. These findings are consistent with the work function analysis. Moreover, the Mulliken charge calculation indicates that electrons are transferred from NiS to WO_3, then the WO_3 obtained 1.52 electrons after contact.

The chemical states of the samples were examined by X-ray photoelectron spectroscopy (XPS). The survey spectrum (Fig. S2) indicates the presence of W, O, Ni, and S in WONS35 %. Fig. 7a displays the W 4 f XPS spectra. Two peaks at approximately 35.2 eV corresponding to W 4 $f_{7/2}$ and 37.3 eV corresponding to W 4 $f_{5/2}$ were observed, indicating presence of W^{6+} in WO_3. The O 1 s XPS spectrum of WO_3 (Fig. 7b) demonstrates the existence of two forms of O species: lattice O (at 530.4 eV) and -OH (at 532.0 eV). Interestingly, the binding energies of W 4 f and O 1 s for WONS35 % exhibit a 0.2 eV shift to lower values compared to

those for WO_3, indicating electron transfer from NiS to WO_3. The same conclusion can be made by examining the Ni 2p and S 2p XPS spectra of WONS35 %. The Ni 2p XPS spectrum of WONS35 % (Fig. 7c) shows Ni $2p_{3/2}$ (856.1 eV) and Ni $2p_{1/2}$ (873.8 eV) as well as their respective satellite peaks (861.7 and 879.6 eV). Both the binding energies of Ni 2p and S 2p (Fig. 7d) for WONS35 % display a positive shift relative to those of pure NiS. The observed shifts in binding energies indicate the formation of a close contact between WO_3 and NiS in WONS35 % [50]. The electron transfer from WO_3 to NiS was further verified by in-situ XPS performed under UV light irradiation. Notably, the binding energies of W 4 f and O 1 s of WONS35 % (Fig. 7a-b) exhibit a positive shift of roughly 0.3 eV compared to those measured without UV light irradiation. Conversely, the binding energies of Ni 2p and S 2p of WONS35 % (Fig. 7c-d) display a shift by 0.4 eV towards lower values under UV irradiation.

To probe the main active species involved in the photocatalytic generation of H_2O_2 over WONS35 %, trapping experiments were conducted and the results are shown in Fig. 8a and Fig. S4, based on which, photogenerated electrons are found crucial. ESR measurements were further conducted to gain a better understanding of the photocatalytic reaction mechanism [60]. The results, as depicted in Fig. 8b and Fig. S5, demonstrate that the DMPO-•O_2 signal can be clearly observed over NiS and WONS35 % but not over WO_3 after 10 min of irradiation, suggesting that the indirect two-electron ORR [Eqs. (4), (5)] is most likely responsive for the formation of H_2O_2.
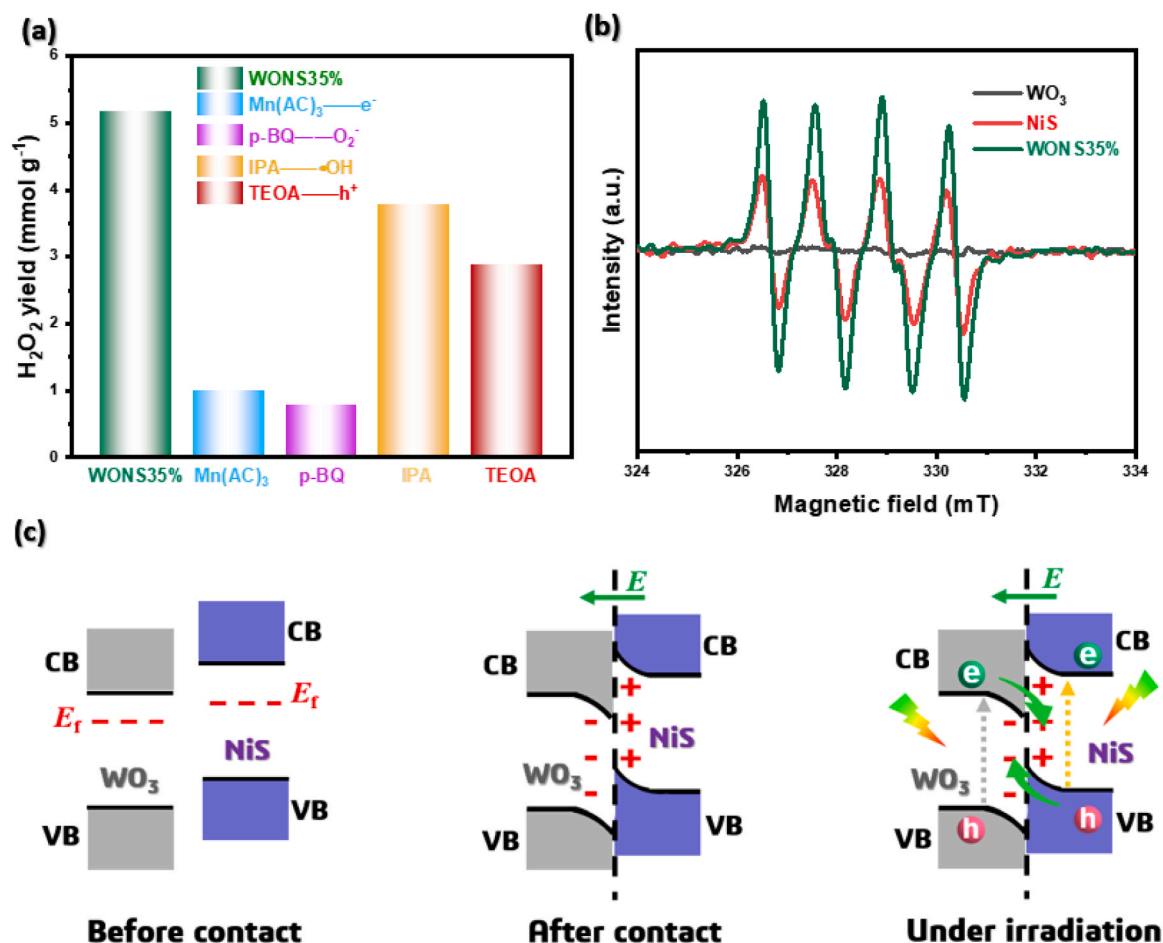
Fig. 8. (a) Effects of H_2O_2 production with addition of different scavengers. (b) EPR spectra of $\bullet O_2^-$ generated over WO_3, NiS and WONS35 % under 10 min irradiation. (c) Schematic illustration of the WO_3/NiS heterojunction: internal electric field (IEF) induced charge transfer, separation, and the formation of step-scheme heterojunction under irradiation.

$$2H^+ + O_2 + 2e^- \rightarrow H_2O_2 \tag{3}$$

$$O_2 + e^- \rightarrow \cdot O_2^- \tag{4}$$

$$\cdot O_2^- + 2H^+ + e^- \rightarrow H_2O_2 \tag{5}$$

Early in-situ XPS measurements and DFT calculations have shown that WO_3 possesses a lower Fermi level than NiS. Once they come close to each other to form a heterojunction, electrons tend to flow from NiS to WO_3, leading to creation of an interfacial electric field (IEF) at the WO_3/NiS interface [61,62]. Therefore, the energy bands of WO_3 and NiS bend. Under illumination, the IEF drives the photogenerated electrons in the CB of WO_3 to flow towards WO_3/NiS interface, where they recombine with the photogenerated holes in the VB of NiS. As a result, NiS becomes electron-rich and serves as reduction sites to reduce molecular O_2, yielding H_2O_2 through a two-electron pathway. The formation of a step-scheme heterojunction between WO_3 and NiS enables fast transport of photogenerated charge carriers to the respective semiconductors, ensuring efficient charge separation while maintaining high redox ability of electrons in NiS CB and holes in WO_3 VB. Therefore, the exceptional photocatalytic performance of the catalyst in this study can be attributed to the step-scheme heterojunction formed between WO_3 and NiS, which enables efficient charge separation and a unique step-scheme pathway for photoreduction and photooxidation.

4. Conclusion

In summary, WO_3/NiS hybrid nanofibers have been prepared by an electrospinning plus hydrothermal method. Driven by the IEF, the photogenerated electrons in the CB of WO_3 recombine with the photogenerated holes in the VB of NiS at the WO_3/NiS interface, as confirmed by in-situ XPS, corroborating a step-scheme charge transfer pathway. The formation of WO_3/NiS step-scheme heterojunction not only enhanced light absorption, prolonged lifetime of photogenerated carriers, but also maintained the strong redox ability of photogenerated carriers. All of which ensured a high photocatalytic performance of the WO_3/NiS hybrid nanofibers. This work presents an interesting contribution to construct all-inorganic step-scheme heterojunctions for economical and efficient production of hydrogen peroxide in pure water under light illumination.

CRediT authorship contribution statement

Kai Wang: Experiment, Data processing & analysis, Writing – original draft, Resources. **Jingping Li:** Experiment, Data processing. **Xiufan Liu:** DFT calculation. **Qiang Cheng:** Data analysis. **Yue Du:** Data analysis. **Dian Li:** Data analysis. **Bin Liu:** Writing – review & editing, Resources.

Declaration of Competing Interest

The authors declare that they have no known competing financial

interests or personal relationships that could have appeared to influence the work reported in this paper.

Data Availability

Data will be made available on request.

Acknowledgments

Appendix A. Supporting information

Supplementary data associated with this article can be found in the online version at doi:10.1016/j.apcatb.2023.123349.

References

[1] S. Song, J. Qu, P. Han, M.J. Hülsey, G. Zhang, Y. Wang, S. Wang, D. Chen, J. Lu, N. Yan, Visible-light-driven amino acids production from biomass-based feedstocks over ultrathin CdS nanosheets, Nat. Commun. 11 (2020) 4899.

[2] X. Zhang, J. Liu, H. Zhang, Z. Wan, J. Li, Uncovering the pathway of peroxymonosulfate activation over $Co_{0.5}Zn_{0.5}O$ nanosheets for singlet oxygen generation: Performance and membrane application, Appl. Catal. B 327 (2023), 122429.

[3] Z. Wang, G. Li, W. Hou, H. Guo, L. Wang, M. Wu, Insights into the use of Te-O pairs as active centers of carbon nanosheets for efficient electrochemical oxygen reduction, ACS Nano 17 (2023) 8671–8679.

[4] M. Fan, Z. Wang, K. Sun, A. Wang, Y. Zhao, Q. Yuan, R. Wang, J. Raj, J. Wu, J. Jiang, L. Wang, N-B-OH site-activated graphene quantum dots for boosting electrochemical hydrogen peroxide production, Adv. Mater. 35 (2023), e2209086.

[5] Z. Wu, J. Shen, W. Li, J. Li, D. Xia, D. Xu, S. Zhang, Y. Zhu, Electron self-sufficient core-shell $BiOCl@Fe$-BiOCl nanosheets boosting Fe(III)/Fe(II) recycling and synergetic photocatalysis-Fenton for enhanced degradation of phenol, Appl. Catal. B 330 (2023), 122642.

[6] K. Wang, H. Qin, J. Li, Q. Cheng, Y. Zhu, H. Hu, J. Peng, S. Chen, G. Wang, S. Chou, S. Dou, Y. Xiao, Metallic $AgInS_2$ nanocrystals with sulfur vacancies boost atmospheric CO_2 photoreduction under near-infrared light illumination, Appl. Catal. B 332 (2023), 122763.

[7] Z. Teng, Q. Zhang, H. Yang, K. Kato, W. Yang, Y. Lu, S. Liu, C. Wang, A. Yamakata, C. Su, B. Liu, T. Ohno, Atomically dispersed antimony on carbon nitride for the artificial photosynthesis of hydrogen peroxide, Nat. Catal. 4 (2021) 374–384.

[8] Z. Teng, N. Yang, H. Lv, S. Wang, M. Hu, C. Wang, D. Wang, G. Wang, Edge-functionalized g-C_3N_4 nanosheets as a highly efficient metal-free photocatalyst for safe drinking water, Chem 5 (2019) 664–680.

[9] L. Li, L. Xu, Z. Hu, J.C. Yu, Enhanced mass transfer of oxygen through a gas-liquid-solid interface for photocatalytic hydrogen peroxide production, Adv. Funct. Mater. 31 (2021), 2106120.

[10] Q. Chen, C. Lu, B. Ping, G. Li, J. Chen, Z. Sun, Y. Zhang, Q. Ruan, L. Tao, A hydroxyl-induced carbon nitride homojunction with functional surface for efficient photocatalytic production of H_2O_2, Appl. Catal. B 324 (2023), 122216.

[11] B. Liu, C. Bie, Y. Zhang, L. Wang, Y. Li, J. Yu, Hierarchically porous ZnO/g-C_3N_4 S-scheme heterojunction photocatalyst for efficient H_2O_2 production, Langmuir 37 (2021) 14114–14124.

[12] W. Liu, P. Wang, J. Chen, X. Gao, H.N. Che, B. Liu, Y. Ao, Unraveling the mechanism on ultrahigh efficiency photocatalytic H_2O_2 generation for dual-heteroatom incorporated polymeric carbon nitride, Adv. Funct. Mater. (2022), 2205119.

[13] X. Zhang, J. Liu, X. Zheng, R. Chen, M. Zhang, Z. Liu, Z. Wang, J. Li, Activation of oxalic acid via dual-pathway over single-atom Fe catalysts: Mechanism and membrane application, Appl. Catal. B 321 (2023), 122068.

[14] P. Ma, X. Zhang, C. Wang, Z. Wang, K. Wang, Y. Feng, J. Wang, Y. Zhai, J. Deng, L. Wang, K. Zheng, Band alignment of homojunction by anchoring CN quantum dots on g-C_3N_4 (0D/2D) enhance photocatalytic hydrogen peroxide evolution, Appl. Catal. B 300 (2022), 120736.

[15] Q. You, C. Zhang, M. Cao, B. Wang, J. Huang, Y. Wang, S. Deng, G. Yu, Defects controlling, elements doping, and crystallinity improving triple-strategy modified carbon nitride for efficient photocatalytic diclofenac degradation and H_2O_2 production, Appl. Catal. B 321 (2023), 121941.

[16] W. Wang, X. Li, F. Deng, J. Liu, X. Gao, J. Huang, J. Xu, Z. Feng, Z. Chen, L. Han, Novel organic/inorganic PDI-Urea/BiOBr S-scheme heterojunction for improved photocatalytic antibiotic degradation and H_2O_2 production, Chin. Chem. Lett. 33 (2022) 5200–5207.

[17] C. Pan, G. Bian, Y. Zhang, Y. Lou, Y. Zhang, Y. Dong, J. Xu, Y. Zhu, Efficient and stable H_2O_2 production from H_2O and O_2 on $BiPO_4$ photocatalyst, Appl. Catal. B 316 (2022), 121675.

[18] W. Liu, P. Wang, J. Chen, X. Gao, H. Che, B. Liu, Y. Ao, Unraveling the mechanism on ultrahigh efficiency photocatalytic H_2O_2 generation for dual-heteroatom incorporated polymeric carbon nitride, Adv. Funct. Mater. 32 (2022), 2205119.

[19] H. Che, X. Gao, J. Chen, J. Hou, Y. Ao, P. Wang, Iodide-induced fragmentation of polymerized hydrophilic carbon nitride for high-performance quasi-homogeneous photocatalytic H_2O_2 production, Angew. Chem. Int. Ed. 60 (2021) 25546–25550.

[20] X. Li, B. Kang, F. Dong, Z. Zhang, X. Luo, L. Han, J. Huang, Z. Feng, Z. Chen, J. Xu, B. Peng, Z. Wang, Enhanced photocatalytic degradation and H_2/H_2O_2 production performance of S-pCN/$WO_{2.72}$ S-scheme heterojunction with appropriate surface oxygen vacancies, Nano Energy 81 (2021), 105671.

[21] Y. Yang, B. Zhu, L. Wang, B. Cheng, L. Zhang, J. Yu, In-situ grown N, S co-doped graphene on TiO_2 fiber for artificial photosynthesis of H_2O_2 and mechanism study, Appl. Catal. B 317 (2022), 121788.

[22] H. Che, J. Wang, X. Gao, J. Chen, P. Wang, B. Liu, Y. Ao, Regulating directional transfer of electrons on polymeric g-C_3N_5 for highly efficient photocatalytic H_2O_2 production, J. Colloid Interface Sci. 627 (2022) 739–748.

[23] H. Cheng, H. Lv, J. Cheng, L. Wang, X. Wu, H. Xu, Rational design of covalent heptazine frameworks with spatially separated redox centers for high-efficiency photocatalytic hydrogen peroxide production, Adv. Mater. 34 (2022), e2107480.

[24] H. Hou, X. Zeng, X. Zhang, Production of hydrogen peroxide by photocatalytic processes, Angew. Chem. Int. Ed. 59 (2020) 17356–17376.

[25] H. Shi, Y. Li, X. Wang, H. Yu, J. Yu, Selective modification of ultra-thin g-C_3N_4 nanosheets on the (110) facet of Au/$BiVO_4$ for boosting photocatalytic H_2O_2 production, Appl. Catal. B 297 (2021), 120414.

[26] T. Liu, Z. Pan, J.J.M. Vequizo, K. Kato, B. Wu, A. Yamakata, K. Katayama, B. Chen, C. Chu, K. Domen, Overall photosynthesis of H_2O_2 by an inorganic semiconductor, Nat. Commun. 13 (2022) 1034.

[27] J. Zhang, J. Lang, Y. Wei, Q. Zheng, L. Liu, Y. Hu, B. Zhou, C. Yuan, M. Long, Efficient photocatalytic H_2O_2 production from oxygen and pure water over graphitic carbon nitride decorated by oxidative red phosphorus, Appl. Catal. B 298 (2021), 120522.

[28] S. Lin, Q. Wang, H. Huang, Y. Zhang, Piezocatalytic and photocatalytic hydrogen peroxide evolution of sulfide solid solution nano-branches from pure water and air, Small 18 (2022), e2200914.

[29] C. Yang, S. Wan, B. Zhu, J. Yu, S. Cao, Calcination-regulated microstructures of donor-acceptor polymers towards enhanced and stable photocatalytic H_2O_2 production in pure water, Angew. Chem. Int. Ed. 61 (2022), e202208438.

[30] G. Han, F. Xu, B. Cheng, Y. Li, J. Yu, L. Zhang, Enhanced photocatalytic H_2O_2 production over inverse opal ZnO@polydopamine S-scheme heterojunctions, Acta Phys. Chim. Sin. 38 (2022), 2112037.

[31] L. Wang, J. Zhang, Y. Zhang, H. Yu, Y. Qu, J. Yu, Inorganic Metal-oxide photocatalyst for H_2O_2 production, Small 18 (2022), e2104561.

[32] Y. Zhang, J. Qiu, B. Zhu, M.V. Fedin, B. Cheng, J. Yu, L. Zhang, ZnO/COF S-scheme heterojunction for improved photocatalytic H_2O_2 production performance, Chem. Eng. J. 444 (2022), 136584.

[33] S. Li, M. Cai, C. Wang, Y. Liu, Ta_3N_5/CdS core-shell S-scheme heterojunction nanofibers for efficient photocatalytic removal of antibiotic tetracycline and Cr (VI): performance and mechanism insights, Adv. Fiber Mater. 5 (2023) 994–1007.

[34] K. Wang, X. Shao, K. Zhang, J. Wang, X. Wu, H. Wang, 0D/3D Bi_3TaO_7/$ZnIn_2S_4$ heterojunction photocatalyst towards degradation of antibiotics coupled with simultaneous H_2 evolution: in situ irradiated XPS investigation and S-scheme mechanism insight, Appl. Surf. Sci. 596 (2022), 153444.

[35] S. Li, C. Wang, Y. Liu, Y. Liu, M. Cai, W. Zhao, X. Duan, S-scheme MIL-101(Fe) octahedrons modified Bi_2WO_6 microspheres for photocatalytic decontamination of Cr(VI) and tetracycline hydrochloride: Synergistic insights, reaction pathways, and toxicity analysis, Chem. Eng. J. 455 (2023), 140943.

[36] X. Shao, K. Wang, L. Peng, K. Li, H. Wen, X. Le, X. Wu, G. Wang, In-situ irradiated XPS investigation on 2D/1D $Cd_{0.5}Zn_{0.5}S$/Nb_2O_5 S-scheme heterojunction photocatalysts for simultaneous promotion of antibiotics removal and hydrogen evolution, Colloids Surf. A 652 (2022), 129846.

[37] S. Li, M. Cai, Y. Liu, C. Wang, R. Yan, X. Chen, Constructing $Cd_{0.5}Zn_{0.5}S$/Bi_2WO_6 S-scheme heterojunction for boosted photocatalytic antibiotic oxidation and Cr(VI) reduction, Adv. Powder Mater. 2 (2023), 100073.

[38] K. Wang, L. Peng, X. Shao, Q. Cheng, J. Wang, K. Li, H. Wang, Nb-O-C charge transfer bridge in 2D/2D Nb_2O_5/g-C_3N_4 S-scheme heterojunction for boosting solar-driven CO_2 Reduction: In situ illuminated X-ray photoelectron spectroscopy investigation and mechanism insight, Sol. RRL 6 (2022), 2200434.

[39] S. Li, M. Cai, Y. Liu, C. Wang, K. Lv, X. Chen, S-scheme photocatalyst TaON/Bi_2WO_6 nanofibers with oxygen vacancies for efficient abatement of antibiotics and Cr(VI): Intermediate eco-toxicity analysis and mechanistic insights, Chin. J. Catal. 43 (2022) 2652–2664.

[40] J. Yang, J. Wang, W. Zhao, G. Wang, K. Wang, X. Wu, J. Li, 0D/1D Cu_{2-x}/TiO_2 S-scheme heterojunction with enhanced photocatalytic CO_2 reduction performance via surface plasmon resonance induced photothermal effects, Appl. Surf. Sci. 613 (2023), 156083.

[41] Q. Wang, G. Wang, J. Wang, J. Li, K. Wang, S. Zhou, Y. Su, In situ hydrothermal synthesis of ZnS/TiO_2 nanofibers S-scheme heterojunction for enhanced photocatalytic H_2 evolution, Adv. Sustain. Syst. 7 (2022), 2200027.

[42] L. Zhang, J. Zhang, H. Yu, J. Yu, Emerging S-scheme photocatalyst, Adv. Mater. 34 (2022), e2107668.

[43] K. Wang, X. Shao, Q. Cheng, K. Li, X. Le, G. Wang, H. Wang, In situ-illuminated X-ray photoelectron spectroscopy investigation of S-scheme Ta_2O_5/$ZnIn_2S_4$ core-shell

hybrid nanofibers for highly efficient solar-driven CO_2 overall splitting, Sol. RRL 6 (2022), 2200736.

[44] K. Wang, H. Qin, X. Shao, L. Jiang, K. Li, J. Wang, L. Zhou, Q. Cheng, G. Wang, H. Wang, Unveiling S-scheme charge transfer pathways in In_2S_3/Nb_2O_5 hybrid nanofiber photocatalysts for low-Concentration CO_2 Hydrogenation, Sol. RRL 7 (2022), 2200963.

[45] X. Wu, G. Chen, J. Wang, J. Li, G. Wang, Review on S-scheme heterojunctions for photocatalytic hydrogen evolution, Acta Phys. Chim. Sin. 39 (2023), 2212016.

[46] W. Li, Y. Deng, L. Luo, Y. Du, X. Cheng, Q. Wu, Nitrogen-doped $Fe_2O_3/NiTe_2$ as an excellent bifunctional electrocatalyst for overall water splitting, J. Colloid Interface Sci. 639 (2023) 416–423.

[47] B. Zhang, G. An, J. Chen, H. Guo, L. Wang, Surface state engineering of carbon dot/carbon nanotube heterojunctions for boosting oxygen reduction performance, J. Colloid Interface Sci. 637 (2023) 173–181.

[48] M. Fan, Z. Wang, Y. Zhao, Q. Yuan, J. Cui, L. Raj, K. Sun, A. Wang, J. Wu, H. Sun, B. Li, L. Wang, J. Jiang, Porous heterostructure of graphene/hexagonal boron nitride as an efficient electrocatalyst for hydrogen peroxide generation, Carbon Energy (2022) 1–14.

[49] M. Gu, Y. Yang, L. Zhang, B. Zhu, G. Liang, J. Yu, Efficient sacrificial-agent-free solar H_2O_2 production over all-inorganic S-scheme composites, Appl. Catal. B 324 (2023), 122227.

[50] F. Xu, L. Zhang, B. Cheng, J. Yu, Direct Z-Scheme TiO_2/NiS Core-shell hybrid nanofibers with enhanced photocatalytic H_2-production activity, ACS Sustain. Chem. Eng. 6 (2018) 12291–12298.

[51] Q. Shang, J. Wang, J. Yang, Z. Wang, G. Wang, K. Wang, X. Wu, J. Li, Photocatalytic hydrogen evolution coupled with tetracycline photodegradation over S-scheme $BaTiO_3/Ag_2S$ dual-function nanofibers: Performance and mechanism, Appl. Surf. Sci. 635 (2023), 157760.

[52] Y. Lin, G. Huang, L. Chen, J. Zhang, L. Liu, Enhanced CO_2 photoreduction by Ni $(OH)_{2-x}/WO_3$ nanofibers with efficient CO_2 activation and charge separation, Adv. Sustain. Syst. 7 (2022), 2200364.

[53] S. Cao, J. Yu, S. Wageh, A.A. Al-Ghamdi, M. Mousavi, J.B. Ghasemi, F. Xu, H_2-production and electron-transfer mechanism of a noble-metal-free $WO_3@ZnIn_2S_4$ S-scheme heterojunction photocatalyst, J. Mater. Chem. A 10 (2022) 17174–17184.

[54] Y. Zhang, C. Pan, G. Bian, J. Xu, Y. Dong, Y. Zhang, Y. Lou, W. Liu, Y. Zhu, H_2O_2 generation from O_2 and H_2O on a near-infrared absorbing porphyrin supramolecular photocatalyst, Nat. Energy 8 (2023) 361–371.

[55] K. Wang, Y. Du, Y. Li, X. Wu, H. Hu, G. Wang, Y. Xiao, S. Chou, G. Zhang, Atomic-level insight of sulfidation-engineered Aurivillius-related $Bi_2O_2SiO_3$ nanosheets enabling visible light low-concentration CO_2 conversion, Carbon Energy 5 (2023), e264.

[56] K. Wang, Q. Wang, K. Zhang, G. Wang, H. Wang, Selective solar-driven CO_2 reduction mediated by 2D/2D $Bi_2O_2SiO_3/MXene$ nanosheets heterojunction, J. Mater. Sci. Technol. 124 (2022) 202–208.

[57] K. Wang, H. Wang, Q. Cheng, C. Gao, G. Wang, X. Wu, Molecular-functionalized engineering of porous carbon nitride nanosheets for wide-spectrum responsive solar fuel generation, J. Colloid Interface Sci. 607 (2022) 1061–1070.

[58] K. Wang, L. Jiang, T. Xin, Y. Li, X. Wu, G. Zhang, Single-atom V-N charge-transfer bridge on ultrathin carbon nitride for efficient photocatalytic H_2 production and formaldehyde oxidation under visible light, Chem. Eng. J. 429 (2022), 132229.

[59] X. Wu, W. Zhang, J. Li, Q. Xiang, Z. Liu, B. Liu, Identification of the active sites on metallic MoO_{2-x} nano-sea-urchin for atmospheric CO_2 photoreduction under UV, visible, and near-infrared light illumination, Angew. Chem. Int. Ed. 62 (2023), e202213124.

[60] K. Wang, L. Jiang, X. Wu, G. Zhang, Vacancy mediated Z-scheme charge transfer in a 2D/2D $La_2Ti_2O_7/g-C_3N_4$ nanojunction as a bifunctional photocatalyst for solar-to-energy conversion, J. Mater. Chem. A 8 (2020) 13241–13247.

[61] Y. Yang, J. Liu, M. Gu, B. Cheng, L. Wang, J. Yu, Bifunctional TiO_2/COF S-scheme photocatalyst with enhanced H_2O_2 production and furoic acid synthesis mechanism, Appl. Catal. B 333 (2023), 122780.

[62] C. Cheng, J. Zhang, B. Zhu, G. Liang, L. Zhang, J. Yu, Verifying the charge-transfer mechanism in S-scheme heterojunctions using femtosecond transient absorption spectroscopy, Angew. Chem. Int. Ed. 62 (2023), e202218688.